remote sensing

Article

A Multi-Objective Quantum Genetic Algorithm for MIMO Radar Waveform Design

Tianqu Liu [1], Jinping Sun [1,*], Guohua Wang [2] and Yilong Lu [3]

[1] School of Electronics & Information Engineering, Beihang University, Beijing 100191, China; tqliu@buaa.edu.cn
[2] Hertzwell Pte Ltd., Singapore 639798, Singapore; wghwood@hotmail.com
[3] School of Electrical and Electronic Engineering, Nanyang Technological University, Singapore 639798, Singapore; eylu@ntu.edu.sg
[*] Correspondence: sunjinping@buaa.edu.cn; Tel.: +86-010-8231-7240

Abstract: Aiming at maximizing waveform diversity gain when designing a phase-coded multiple-input multiple-output (MIMO) radar waveform set, it is desirable that all waveforms are orthogonal to each other. Hence, the lowest possible peak cross-correlation ratio (*PCCR*) is expected. Meanwhile, low peak auto-correlation side-lobe ratio (*PASR*) is needed for good detection performance. However, it is difficult to obtain a closed form solution to the waveform set from the expected values of the *PASR* and *PCCR*. In this paper, the waveform set design problem is modeled as a multi-objective, NP-hard constrained optimization problem. Unlike conventional approaches that design the waveform set through optimizing a weighted sum objective function, the proposed optimization model evaluates the performance of multi-objective functions based on Pareto level and obtains a set of Pareto non-dominated solutions. That means that the MIMO radar system can trade off each objective function for different requirements. To solve this problem, this paper presents a multi-objective quantum genetic algorithm (MoQGA) based on the framework of quantum genetic algorithm. A new population update strategy for the MoQGA is designed based on the proposed model. Compared to the state-of-the-art methods, like BiST and Multi-CAN, the *PASR* and *PCCR* metrics of the waveform set are 0.95–3.91 dB lower with the parameters of the numerical simulation. The MoQGA is able to minimize *PASR* and *PCCR* of the MIMO radar waveform set simultaneously.

Keywords: MIMO radar; correlation function; multi-objective optimization; orthogonal waveform set design; quantum genetic algorithm

check for updates

Citation: Liu, T.; Sun, J.; Wang, G.; Lu, Y. A Multi-Objective Quantum Genetic Algorithm for MIMO Radar Waveform Design. *Remote Sens.* **2022**, *14*, 2387. https://doi.org/10.3390/rs14102387

Academic Editors: Konrad Jędrzejewski and Matthias Weiß

Received: 2 April 2022
Accepted: 14 May 2022
Published: 16 May 2022

1. Introduction

Radar transmits electromagnetic waves [1–3] and receives echoes to get information about the targets. Radar waveforms determine the modulation of electromagnetic waves transmitted by radar systems. Strictly speaking, designing a radar waveform should properly consider the electromagnetic wave Doppler effects, propagation effects, clutters, etc. However, sometimes the actual electromagnetic environment is complex and changeable [4–6]. Considering all of these factors makes waveform design complicated in the case of MIMO radar. Appropriate MIMO radar waveform models and designing methods are worth studying.

MIMO radar transmits a set of waveforms at multiple transmitters and processes the echo signals received at multiple receivers using a bank of matched filters. The input signal to each matched filter is the superimposed echoes of all transmit signals. Except for the echo of the associated transmit signal that matches the filter, the echoes of the remaining transmit signals are considered as clutters. The essence of pulse radar matched filtering is aperiodic correlation operation. If any two transmit signals are ideally orthogonal, the peak amplitude of the cross-correlation function is zero. Consequently, the waveforms after the matched filtering are perfectly separated, and the MIMO radar waveform diversity gain is maximized. Otherwise, the matched filter bank will not be able to completely separate the waveforms, which will decrease the MIMO radar waveform diversity gain. The ideal orthogonality of the waveform set cannot be realized since the pulse length and bandwidth of an actual radar system are limited [7,8]. Another important performance metric of a MIMO radar waveform set is the peak of auto-correlation function side-lobe, which measures the radar detection performance and is critical for low probability of intercept (LPI) [9–11]. In short, a good MIMO radar waveform set design should have the lowest possible auto-correlation side-lobe peak and cross-correlation peak [12–14].

The transmit signals modulated by constant modulus phase code sequences are the most suitable waveforms for MIMO radar applications. Sarwate [15] and Welch [16] proposed the lower bounds of its correlation functions. Current research on MIMO radar phase-coded waveform design focuses on meeting the lower bounds [17]. Although it is impossible to solve the reverse problem of MIMO waveform design directly from the required correlation functions, many studies have constructed code sequence sets that are close to the lower bound of the periodic cross-correlation peak, which are called CAZAC (Constant Amplitude Zero Auto-correlation Code). However, the sequence sets meeting the lower bound of the aperiodic cross-correlation peak have not been found thus far. Some researchers evaluate aperiodic correlation functions of the CAZAC sequence set [18,19] with the results showing that the performance of the aperiodic cross-correlation function of the CAZAC sequence set is relatively good but it is also far from the bound.

Aiming at achieving good LPI performance and high MIMO diversity gain simultaneously, the peak auto-correlation side-lobe ratio (*PASR*), the peak cross-correlation ratio (*PCCR*), and the integrated side-lobe level (*ISL*) should be minimized. Meanwhile, due to the conflict between *PASR*, *PCCR* and *ISL*, the MIMO radar waveform set design problem is modeled as a Pareto optimization problem involving multiple objective functions. The problem is difficult because it is NP-hard with non-convex multiple objective functions.

There are lot of works on designing phase code sequence set for MIMO radar using specially designed numerical optimization algorithms [20–26], including the popular Multi-CAN [20], MM-Corr [21], and ISL-New [22] algorithms. These algorithms in general reformulate the original multi-objective optimization problem into relaxed single objective problem with good local convergence properties that are easily solvable via iterative algorithms. Those iterative algorithms almost all reach the lower bound of the *ISL*. However, none of them could reach the lower bound of *PASR* and *PCCR*. The new BiST [27] algorithm outstrips all the above algorithms under some sequence lengths and set sizes, but its performance is also not good enough when optimizing the *PCCR*. In particular, the BiST algorithm models its objective function as an adjustable weighted sum of the multi-objective functions, which cannot decrease the values of each objective function strictly.

In contrast to the abovementioned methods, evolutionary algorithms are highly robust and widely applicable to global search problems [28–32]. They are capable of solving high-dimensional optimization problems [33–35] and have been applied to waveform design problems [36–40]. There are few works on MIMO radar waveform set design using a multi-objective evolutionary model. QGA can converge faster while ensuring good population diversity, improving the search efficiency. However, there is no universal multi-objective QGA algorithm framework, which is different for different applications [41–44]. Quantum chromosome encoding, quantum rotation and the population update strategy of the QGA are not suitable for multi-objective optimization problems because the optimal solution at the end of each generation is replaced by a set of non-dominated solutions.

This paper develops a multi-objective quantum genetic algorithm (MoQGA), based on the framework of quantum genetic algorithm (QGA) [31], to solve the above-mentioned Pareto optimization problem. In this paper, a quantum chromosome encoding and decoding for the waveform set is constructed. This paper designs a quantum rotation targets selection strategy based on Pareto dominance. After designing all the sub-steps of the MoQGA properly, the population update strategy is constructed.

The values of the *PASR* and *PCCR* metrics obtained by the proposed method are 0.95–3.91 dB lower than the state-of-the-art methods like Multi-CAN [20] and BiST [27].

The obtained *ISL* metric values are close to the lower bound. Furthermore, a large number of trials prove that the stability of the MoQGA is good. The MoQGA is able to design a MIMO radar phase-coded waveform set with low correlation functions stably.

The rest of this paper is organized as follows. Section 2 states the MIMO radar waveform set design problem. Section 3 shows the implementation of the MoQGA. Section 4 shows some numerical results. Finally, Section 5 concludes the paper.

2. Problem Statement

2.1. MIMO Radar Phase-Coded Waveform Set

Consider a MIMO radar waveform set with M transmit signals showed in Figure 1. The transmitted waveform set $S(t)$ can be expressed as

$$S(t) = [s_1(t), s_2(t), \ldots, s_M(t)] \tag{1}$$

where $s_m(t),\ m = 1, 2, \ldots, M$ is the m-th transmit signal.

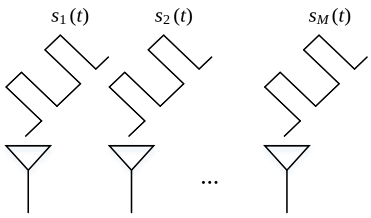

Figure 1. MIMO radar with M transmit signals.

In this paper, only phase-coded waveform set is discussed. Phase-coded waveform has constant amplitude and RF frequency in the pulse duration, and the signal within the pulse duration is modulated by a phase code sequence. The sequence length N represent the number of sub-pulses (chips). The pulse length is τ and sub-pluses length is τ_c. They satisfy the condition $\tau = N\tau_c$. The analog signal of the waveform can be expressed as

$$s_m(t) = \sum_{n=0}^{N-1} x_n^m(t - n\tau_c) \cdot U(t), 0 \le t \le \tau \tag{2}$$

$$x_n^m(t) = \begin{cases} x_m[n] = \exp(j\phi_m[n]), & 0 \le t \le \tau_c \\ 0, & \text{others} \end{cases} \tag{3}$$

where $\phi_m[n] \in [0, 2\pi], n = 1, 2, \ldots, N$. $x_m[n]$ is the phase code sequence and $U(t)$ is the radio frequency carrier signal. Normally, the phase value is set to one of K constant values between 0 and 2π. Then the phase values set Ψ can be defined as

$$\begin{aligned} \Psi &= \{0, 2\pi/K, 4\pi/K, \ldots, 2\pi(K-1)/K\} \\ &= \{\phi | \phi = 2\pi(k-1)/K\},\ k = 1, 2, 3, \ldots, K \end{aligned} \tag{4}$$

where K is a positive integer no smaller than 2. The phase code matrix X can be defined as follow, which is made up by M phase code sequences.

$$X = \begin{bmatrix} x_{11} & x_{12} & \cdots & x_{1N} \\ x_{21} & x_{22} & \cdots & x_{2N} \\ \vdots & \vdots & \ddots & \vdots \\ x_{M1} & x_{M2} & \cdots & x_{MN} \end{bmatrix} \tag{5}$$

where $x_{mn} = x_m[n]$. X is exactly the decision variable for the MIMO radar phase-coded waveform set optimization design problem. The solution space is the set of all possible phase code matrix X. So, the solution space Ω can be described as

$$\begin{cases} X \in \Omega,\ x_{ij} = \exp(j\varphi_{ij}),\ i,j \in \{1,2,\ldots,M\} \\ \varphi_{ij} \in \{\phi | \phi = 2\pi(k-1)/K, k = 1,2,\ldots,K\} \end{cases} \tag{6}$$

2.2. Performance Evaluation Metrics

According to the signal model of the waveform set $S(t)$, the phase-coded waveform set $S(t)$ is jointly determined by the phase code matrix X mentioned above, carrier frequency, pulse length, etc. Compared to carrier frequency, pulse length and other hardware parameters, phase code matrix X is the key factor that determines the performance of correlation functions of MIMO waveform set [45]. Specifically, the aperiodic auto- and cross-correlation function between the phase-coded sequences are defined as

$$r_i^{AP}[k] = \sum_{n=1}^{N-k} x_i[n] x_i^*[n+k]\ i \in \{1,2,\ldots,M\} \tag{7}$$

$$r_{ij}^{AP}[k] = \sum_{n=1}^{N-k} x_i[n] x_j^*[n+k]\ i,j \in \{1,2,\ldots,M\} \tag{8}$$

where k is an integer with $-N < k < N$, $(\cdot)^*$ is complex conjugate. When $k = 0$, the aperiodic auto-correlation function takes the peak value, which is also called the main-lobe peak. Since the amplitude of the phase code sequences is a constant, it is obvious that $\left|r_i^{AP}[0]\right| = N, i \in \{1,2,\ldots,M\}$. When $k \neq 0$, the rest part of the auto-correlation function is called the side-lobe. The following three metrics are defined to evaluate the performance of the auto- and cross-correlation function.

$$PCCR = \frac{1}{N^2} \max_{\substack{i,j \\ i \neq j}} \left\{ \max_k \left|r_{ij}[k]\right|^2 \right\} \tag{9}$$

$$PASR = \frac{1}{N^2} \max_i \left\{ \max_{k,k\neq 0} \left|r_i[k]\right|^2 \right\} \tag{10}$$

$$ISL = \frac{1}{N^2} \left(\sum_{\substack{i,j=1 \\ i \neq j}}^{M} \sum_{k=-N+1}^{N-1} \left|r_{ij}[k]\right|^2 + \sum_{i=1}^{M} \sum_{\substack{k=-N+1 \\ k \neq 0}}^{N-1} \left|r_i[k]\right|^2 \right) \tag{11}$$

where $PCCR$ means peak cross-correlation ratio, $PASR$ means peak auto-correlation side-lobe ratio and ISL means integrated side-lobe level. Since this paper does not discuss the periodic correlation functions, $r_{ij}[k]$ is regarded as $r_{ij}^{AP}[k]$. $PCCR$ measures the degree of mutual interference between the different transmit signals. $PASR$ measures the ratio between the side-lobe peak and the main-lobe after the pulse compression. ISL measures the summation of the auto-correlation function side-lobe and the cross-correlation function. The lower the values of these three metrics, the better the MIMO radar waveform set performance.

Because of the limited pulse length and bandwidth, these metrics cannot be infinitely small. Sarwate [15] and Welch [16] deduced the lower bounds for $PCCR$, $PASR$ and ISL. In their derivation, $PCCR$ and $PASR$ were combined into one metric called peak side-lobe level, $PSL = \max\{PCCR, PASR\}$. The lower bounds of the PSL and ISL under periodic and aperiodic conditions are shown as follows.

$$PSL^P \geq Bound_{PSL}^P = \frac{M-1}{NM-1} \tag{12}$$

$$PSL^{AP} \geq Bound_{PSL}^{AP} = \frac{M-1}{2NM-M-1} \tag{13}$$

$$ISL^P, ISL^{AP} \geq Bound_{ISL} = M(M-1) \tag{14}$$

2.3. Multi-Objective Optimization Model

PSL is the most widely used metric for the MIMO radar waveform set design. However, when *PSL* reach the optimal value, there is no guarantee that *PASR* and *PCCR* will reach the optimal values. Actually, *PASR* and *PCCR* are two conflicting metrics. Moreover, the *ISL* measures the overall performance of the auto- and cross-correlation functions. Hence, modeling the MIMO radar phase-coded waveform set design problem as a multi-objective Pareto optimization problem is a more rigorous way. Based on the definition of the solution space Ω in (6), the multi-objective functions are shown as follows.

$$f_1(X) = PCCR(X) = \frac{1}{N^2} \max_{\substack{i,j \\ i \neq j}} \left\{ \max_k \left| \sum_{n=1}^{N-l} x_{i,n} x_{j,n+k}^* \right|^2 \right\} \tag{15}$$

$$f_2(X) = PASR(X) = \frac{1}{N^2} \max_i \left\{ \max_{k,k\neq 0} \left| \sum_{n=1}^{N-l} x_{i,n} x_{i,n+k}^* \right|^2 \right\} \tag{16}$$

$$f_3(X) = ISL(X) = \frac{1}{N^2} \left(\sum_{\substack{i,j=1 \\ i \neq j}}^{M} \sum_{k=-N+1}^{N-1} \left| \sum_{n=1}^{N-l} x_{i,n} x_{j,n+k}^* \right|^2 + \sum_{i=1}^{M} \sum_{\substack{k=-N+1 \\ k \neq 0}}^{N-1} \left| \sum_{n=1}^{N-l} x_{i,n} x_{i,n+k}^* \right|^2 \right) \tag{17}$$

In summary, the MIMO phase-coded waveform set design problem can be modeled as a multi-objective optimization problem. According to the definition of the solution space and three objective functions, the optimization problem can be formulated as

$$\begin{aligned} &\min_X \mathcal{F}(X) = (f_1(X), f_2(X), f_3(X)) \\ &\text{s.t.} X = \begin{bmatrix} x_{11} & x_{12} & \cdots & x_{1N} \\ x_{21} & x_{22} & \cdots & x_{2N} \\ \vdots & \vdots & \ddots & \vdots \\ x_{M1} & x_{M2} & \cdots & x_{MN} \end{bmatrix} \in \Omega \\ &x_{ij} = \exp(j\varphi_{ij}) \\ &\varphi_{ij} \in \{\phi \mid \phi = 2\pi(k-1)/K, k = 1, 2, \ldots, K\} \end{aligned} \tag{18}$$

where $f_k(X)$ (k = 1, 2, 3) are the objective functions, X the decision variable, Ω the solution space of X, and K represents the phase-coded waveform set is modulated by sequences with K phases.

3. Multi-Objective Quantum Genetic Algorithm

Observing the multi-objective optimization problem model described in (15)–(18), the matrix dimension of X is large. For the parameters M, N, K, there are a total of K^{MN} different phase code matrices, and it is impossible to traverse all the possible solutions. According to the expressions of the three objective functions, it is not difficult to discover that every objective function is non-convex. Hence, designing the phase-coded waveform set is a NP-hard non-convex optimization problem. Current mature convex optimization algorithms are difficult to be applied to this problem. From another point of view, the problem can also be seen as a minimax problem. However, due to the complexity and non-linear characteristics of the objective functions, the existing algorithms against the minimax problem do not work well either [46].

Consider the nature of this multi-objective optimization problem, using evolutionary algorithms is a straightforward yet effective way to solve it. Evolutionary algorithms such as particle swarm optimization (PSO) [47] and genetic algorithm have no special requirements for the objective function. The randomness and diversity of the population reduce the possibility of the algorithm falling into a local optimum. Under the framework of multi-objective evolutionary optimization, Pareto dominance [28] is used to evaluate objective functions. Although the evolutionary algorithm is robust and suitable for solving complex multi-objective optimization problems, its convergence speed is slow. Learning from quantum genetic algorithm (QGA) [31], using quantum chromosome to encode the phase code matrix may improve the algorithm execution speed. Moreover, because of the implicit parallelism, the quantum evolutionary algorithm is easy to be implemented on parallel computer system.

In order to solve the problem of designing the constant modulus waveform set, this paper proposes a multi-objective quantum genetic algorithm (MoQGA) based on the framework of multi-objective optimization and QGA. In particular, this paper has designed the quantum chromosome encoding of the phase code matrix. Using quantum-rotating gate, a novel rotating targets selection strategy is designed for MoQGA. Based on the quantum chromosome and Pareto dominance, the population update strategy is developed.

The block diagram of MoQGA is shown in Figure 2. In addition, the specific execution steps are summarized as follows.

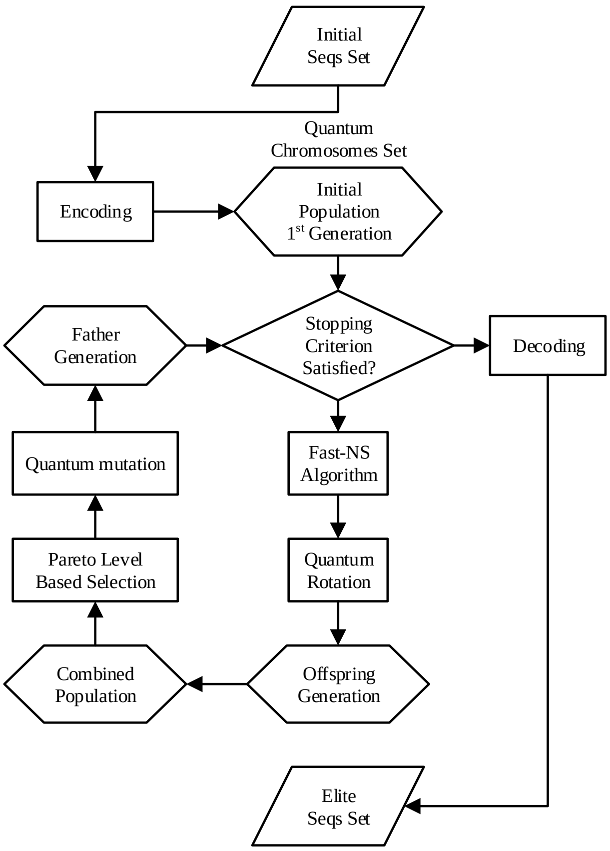

Figure 2. Framework of MoQGA for MIMO radar phase-coded waveform set design.

Step 1 Generate phase code matrix of the size $M \times N$ using random numbers.

Step 2 Initialize the first-generation population, encode the phase code matrix into quantum chromosomes (the population size is set to 100).

Step 3 Use fast Pareto non-dominated sorting (Fast-NS) algorithm [29] to evaluate the first-generation population generated by Step 2. The output of the algorithm is the Pareto level of each individual in the population. Record the Pareto dominance relationship between any two individuals.

Step 4 According to the sorting result of Step 3, update the population and obtain the offspring population using quantum rotate gate.
Step 5 Combine the parent and offspring population, and use the Fast-NS algorithm to sort the combined population.
Step 6 According to the result of Step 5, select appropriate number of elite individuals to form new parent population.
Step 7 Perform quantum mutation operation on the new parent population to increase population diversity.
Step 8 Check whether the maximum genetic generation is reached, if yes, output the elite population and decode it into the phase code matrices, otherwise jump to Step 3 and continue execution.

3.1. Quantum Chromosome Encoding

Quantum chromosomes use qubit encoding. A system with k qubits is described as

$$\begin{bmatrix} \alpha_1|\alpha_2|\ldots|\alpha_k \\ \beta_1|\beta_2|\ldots|\beta_k \end{bmatrix}, \quad i = 1,2,\ldots,k \tag{19}$$

where α_i and β_i are two complex numbers, which represent the probability amplitude of the i-th qubit. Their modulus satisfies the normalization condition $|\alpha_i|^2 + |\beta_i|^2 = 1$. The $|\alpha_i|^2$ is the probability of discovery $|0\rangle$ during one measurement, and the $|\beta_i|^2$ is the probability of discovery $|1\rangle$. Before calculating the values of multi-objective functions and Pareto level, MoQGA needs to measure the quantum chromosome at first. Then decode the measured binary result into decision variables. Finally, calculate the value of the multi-objective function using the decision variables. When the MoQGA is executed to a certain preset maximum generation or the probability amplitude α_i, β_i satisfies $\alpha_i = 1, \beta_i = 0$ or $\alpha_i = 0, \beta_i = 1$, the algorithm stops.

After the decision variable of the optimization problem is encoded into a quantum chromosome, the update and mutation of the population can be completed using quantum rotate gates and quantum mutation operations. For the MIMO radar phase-coded waveform set design problem described in (18), the decision variable of the MoQGA is a K-phase encoded phase matrix. Therefore, any element of the phase code matrix needs to be encoded with $\log_2 K$ qubits. Therefore, a code matrix of size $M \times N$ can be encoded as a quantum chromosome containing $M \times N \times \log_2 K$ qubits. The quantum chromosome X_{qubit} corresponding to the phase code matrix X can be expressed as follow.

$$\begin{gathered} X_{qubit} = \begin{bmatrix} \alpha_1 \,|\, \alpha_2 \,|\, \ldots \,|\, \alpha_{M\times N\times \log_2 K} \\ \beta_1 \,|\, \beta_2 \,|\, \ldots \,|\, \beta_{M\times N\times \log_2 K} \end{bmatrix} \\ |\alpha_i|^2 + |\beta_i|^2 = 1, i = 1,2,\ldots, M\times N\times \log_2 K \end{gathered} \tag{20}$$

when the probability amplitude has converged, the measured result of X_{qubit} is shown in (21). Because the $M \times N \times \log_2 K$ values are binary number 0 or 1, every $\log_2 K$ bits are convert to decimal number to obtain the phase values.

$$\overline{X}_{qubit} = \left[x_1 \,|\, x_2 \,|\, \ldots \,|\, x_{\log_2 K} \,|\, \ldots\ldots \,|\, x_{M\times N\times \log_2 K} \right] \tag{21}$$

3.2. Pareto Level of Population

For multi-objective functions, MoQGA uses Pareto level as the evaluation criterion for the merits of individuals in the population. Before defining the Pareto level of the finite population, Pareto optimal solution and Pareto front of the solution space are introduced firstly. Let Ω be the solution space, and n is the number of the objective functions. For any two solutions X_a and X_b from Ω, if the following two conditions are true, and then X_a dominates X_b, denoted as $X_a \succ X_b$.

(1) $\forall i = 1, 2, \ldots, n, f_i(X_a) \leq f_i(X_b)$;
(2) $\exists i = 1, 2, \ldots, n, f_i(X_a) < f_i(X_b)$;

If a certain solution $X^* \in \Omega$ satisfies:X^* dominates all other feasible solutions in Ω, then X^* is called non-dominated solution or Pareto optimal solution. Any two Pareto optimal solutions do not dominate each other, and the set of all Pareto optimal solutions is denoted as P^*.

$$P^* \triangleq \{X^* | \neg \exists X \in \Omega : X \succ X^*\} \tag{22}$$

Pareto front PF^* is the front surface of the objective function vectors corresponding to all Pareto optimal solutions, which can be expressed as

$$PF^* = \{\mathcal{F}(X^*) = (f_1(X^*), \ldots, f_n(X^*)) | X^* \in P^*\} \tag{23}$$

Let $S = \{X_1, X_2, \ldots, X_P\}$ be the population of each generation in MoQGA, where P is the number of individuals in each generation population. Similar to the Pareto front of Ω, there is also a Pareto front, denoted by PF_S defined on the population S.

$$\begin{cases} PF_S = \{\mathcal{F}(X^*) = (f_1(X^*), \ldots, f_n(X^*)) \big| X^* \in P_S^*\} \\ P_S^* = \{X^* | \neg \exists X \in S : X \succ X^*\} \end{cases} \tag{24}$$

The purpose of multi-objective optimization is to make PF_S as close as possible to PF^*. Ideally, the Pareto front of the elite population finally obtained by MoQGA algorithm is located on the Pareto front of solution space Ω, denoted by PF_S^*. That means PF_S^* is a subset of PF^*. Take two objective functions as an example for better visualization. As shown in Figure 3, the two coordinate axes represent two objective functions. The area enclosed by the bottom left solid line and the top right dashed line represents the solution space Ω, and the bottom left solid line is Pareto front PF^*. The solid dots represent PF_S, the Pareto front of population with finite size. The hollow dots represent PF_S^*, the ideal Pareto front of population. MoQGA and other multi-objective optimization algorithms expect that the obtained Pareto front have more elements in the Pareto front. At the same time, the more even the distribution, the better the optimization effect.

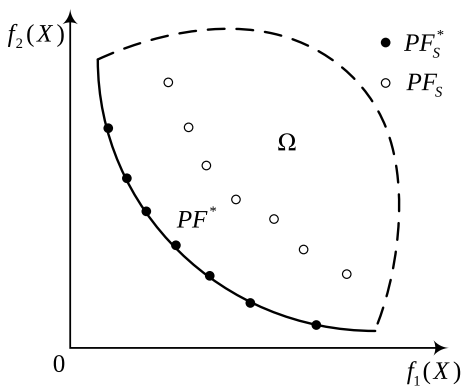

Figure 3. Pareto front of population.

Because the number of solutions in the population S is finite, the Pareto levels can be defined among every solution in S. The set of individuals whose Pareto level are 1 is actually the Pareto front of S.

$$\begin{cases} P_1 = PF_S = \{\mathcal{F}(X^*) = (f_1(X^*), \ldots, f_n(X^*)) \big| X^* \in P_S^*\} \\ P_S^* = \{X^* | \neg \exists X \in S : X \succ X^*\} \end{cases} \tag{25}$$

In (25), P_1 represents the set of individuals whose Pareto level is 1. Remove the individuals of P_1 from the population S, and the Pareto front of the remaining population $S - P_1$ are defined as P_2.

$$P_2 = PF_{S-P_1} \quad (26)$$

Similarly, the Pareto levels of all solutions in this population can be obtained, and the recurrence relationship is shown as follows.

$$P_{level} = PF_{S'} \quad (27)$$

$$S' = S - \sum_{i=1}^{level-1} P_i \quad (28)$$

In (27) and (28), S' is the remaining population set without the individuals whose Pareto level is $1, 2, \ldots, level - 1$. And the Pareto front of S' is the set of individuals whose Pareto level is *level*. Because the number of individuals of S is finite, the number of Pareto levels is also finite. The schematic diagram of the Pareto level is shown in Figure 4. Assuming there are only three Pareto levels in S. The set of all points represents the entire population S, the black solid dots represent P_1, the solid line and open dots represent P_2, and the dashed open dots represent P_3. Generally, the Pareto front, P_1 of the population S, is the optimal solutions and P_2, P_3 and others are suboptimal solutions.

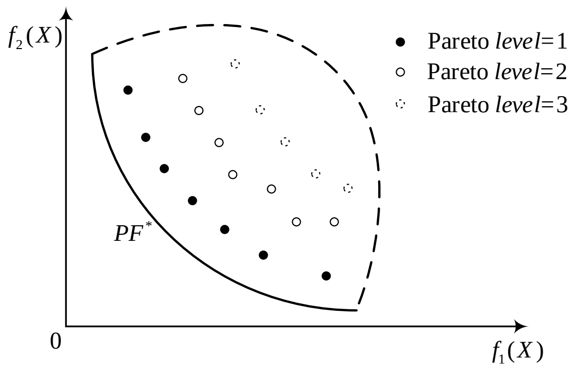

Figure 4. Pareto levels of population.

MoQGA needs to calculate Pareto levels for each generation of the population. In order to improve the execution speed of the algorithm, we use the fast Pareto non-dominated sorting algorithm in NSGA-II [29] to divide the Pareto level. For population $S = \{X_1, X_2, \ldots, X_p, \ldots, X_P\}$ and objective functions $\mathcal{F}(X) = (f_1(X), f_2(X), \ldots, f_n(X))$, the steps of fast non-dominated sorting algorithm for MoQGA are shown in Algorithm 1.

Algorithm 1: Fast non-dominated sorting algorithm for MoQGA

Input: Population set $S = \{X_1, X_2, \ldots, X_p, \ldots, X_P\}$
Objective functions $\mathcal{F}(X) = (f_1(X), f_2(X), \ldots, f_n(X))$
Output: Pareto levels $P_1, P_2, \ldots \ldots$

Step 1: Calculate the dominated number n_p of every individual p. Calculate the set of individuals dominated by p, denoted as U_p. Calculate the set of individuals who dominate p, denoted as D_p.
Step 2: Put the individuals who satisfy $n_p = 0$ into P_1 and set *level* = 1.
Step 3: For every individual $X_p \in P_{level}$

For every individual $X_q \in U_p$
$n_q = n_q - 1$;
If $n_q = 0$
Put X_q into set $P_{level+1}$;

Step 4: $level = level + 1$; Jump to Step 3 to execute; if all the population levels are divided, jump out of the loop and end.

3.3. Population Update Strategy Based on Pareto Levels

The population update strategy of the MoQGA is described as follows. Firstly, combine the offspring population and its parent population when the offspring population is generated. Secondly, select the same number of elite individuals as parent population from the combined population, according to the Pareto level of combined population. And the new parent population is obtained. Thirdly, use quantum rotate gate to update all individuals in the parent population (the rotation strategy is shown later in this paper). Finally, the new offspring population is obtained after quantum mutation operation.

The schematic diagram of the selection strategy is shown in Figure 5, where F_g is the parent population, S_g is the offspring population, P is the population size, and g represents the current generation. Firstly, combine F_g and S_g into population C. Then, execute the fast Pareto non-dominated sorting algorithm on population C, and the Pareto levels of all individuals are obtained. Next, according to the order of Pareto levels from low to high, put the individuals into the new parent population F_{g+1}. Finally, when a certain layer of individuals cannot be completely put into the parent population F_{g+1}, randomly select individuals from this layer to fill up the new parent population F_{g+1}.

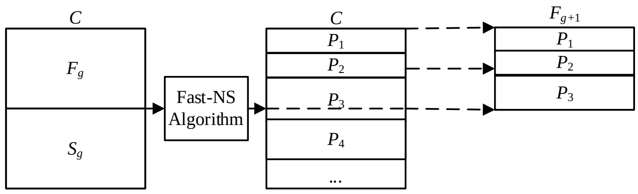

Figure 5. Selection strategy of elite individuals in the population.

3.4. Offspring Population Creation Using Quantum Rotate Gate

MoQGA uses quantum rotate gates to update each individual in the parent population F_{g+1}. The rotation strategy is based on the Pareto dominance relationship obtained by the fast Pareto non-dominated sorting algorithm.

Quantum gates are used to change the probability amplitude of each qubit. Widely used quantum gates include: NOT gates, XOR gates, controlled XOR gates and rotate gates [48]. The generation of the offspring population is based on quantum rotate gates in MoQGA. For the quantum chromosome shown in (20), the quantum rotate gate $U(\theta)$ with a rotation angle θ can be expressed as follow.

$$U(\theta) = \begin{bmatrix} \cos\theta & -\sin\theta \\ \sin\theta & \cos\theta \end{bmatrix} \tag{29}$$

One qubit in quantum chromosome is $x_i = (\alpha_i, \beta_i)^T$, and the process of quantum rotation is

$$x_i' = \begin{bmatrix} \alpha_i' \\ \beta_i' \end{bmatrix} = U(\theta) \cdot \begin{bmatrix} \alpha_i \\ \beta_i \end{bmatrix} = \begin{bmatrix} \cos\theta & -\sin\theta \\ \sin\theta & \cos\theta \end{bmatrix} \cdot \begin{bmatrix} \alpha_i \\ \beta_i \end{bmatrix} \tag{30}$$

where $x_i' = [\alpha_i' \ \beta_i']^T$ is the qubit after the quantum rotation. As known from (30), the direction and size of the rotation angle θ need to be determined before performing the quantum rotation operation. This paper proposes a rotation strategy based on the Pareto dominance of the population.

Determine the individual's rotation target at first, and then calculation the direction and size of rotation angle. Figure 6 shows how to determine the rotation target. The hollow dots in this figure represent the individuals other than Pareto front. The star represents the individual X need to be rotated. P_1 in this figure represents Pareto front of the current population, and PF^* represents Pareto front of the solution space. The p_1, p_2, p_3 in Figure 6 are the available rotating targets of X. They meet two conditions, one is that they all dominate X, and the other is that they are all located on the Pareto front. The set of available rotate targets can be expressed as $B_X = \{p | p \succ X, p \in P_1\}$. Any element of B_X is non-dominated with each other. So, MoQGA randomly selects an individual from it as the rotating target of X, denoted as $b(X)$.

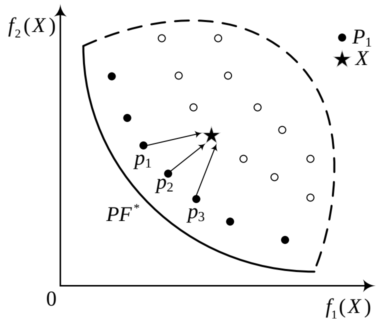

Figure 6. The rotating targets of quantum rotation.

Then, perform a measurement on the quantum chromosome of the individual X and its rotating target $b(X)$. The measured result is expressed as

$$\overline{X} = \left[x_1 \mid x_2 \mid \cdots \mid x_i \mid \cdots \mid x_{M\times N\times \log_2 K}\right] \tag{31}$$

$$b(\overline{X}) = \left[b_1 \mid b_2 \mid \cdots \mid b_i \mid \cdots \mid b_{M\times N\times \log_2 K}\right] \tag{32}$$

where the value of x_i and b_i is 0 or 1. The direction and size of rotation angle $\theta_i = s(\alpha_i, \beta_i) \cdot \Delta\theta_i$ can be determined according to the measurement result, where α_i, β_i are the probability amplitude of the quantum chromosome in (20). The size of the rotation angle is a constant, named rotation step $\Delta\theta_i$. The direction of the rotation angle is controlled by $s(\alpha_i, \beta_i)$, whose available values are $\{-1, 0, 1\}$. They correspond to counterclockwise rotation, no rotation and clockwise rotation respectively. Table 1 describes how to determine the rotation angle. $\delta \in (0, 2\pi)$ represents the value of rotation step. Use a small δ will reduce the convergence speed but may obtain better solutions. Because obtaining waveform set with better metrics have a higher priority, we set $\delta = 0.1\pi$ in this paper.

Table 1. Rotation angle selection strategy.

x_i	b_i	$\Delta\theta_i$	$s(\alpha_i,\beta_i)$			
			$\alpha_i\beta_i > 0$	$\alpha_i\ \beta_i < 0$	$\alpha_i = 0$	$\beta_i = 0$
0	0	0	—	—	—	—
0	1	δ	−1	0	±1	0
1	0	δ	0	−1	0	±1
1	1	0	—	—	—	—

3.5. Quantum Mutation

The last step to generate the offspring population is quantum mutation. Quantum mutation can improve the diversity of the population and enhance the local search ability of MoQGA. In this paper, a quantum mutation operation is designed based on the quantum NOT gate. The steps are as follows.

Step 1 Select several individuals from the population based on a certain probability P_m.
Step 2 Determine several qubits for the selected individuals according to a certain probability P_b.
Step 3 Perform quantum NOT gate operation on the selected qubits.

Among them, P_m is the individual mutation probability; P_b is the qubit mutation probability. They are both constants. The operation of the quantum NOT gate in Step 3 can be expressed by the following formula.

$$x_i' = \begin{bmatrix} \alpha_i' \\ \beta_i' \end{bmatrix} = \begin{bmatrix} \beta_i \\ \alpha_i \end{bmatrix} = \begin{bmatrix} 0 & 1 \\ 1 & 0 \end{bmatrix} \cdot \begin{bmatrix} \alpha_i \\ \beta_i \end{bmatrix} \tag{33}$$

where $x_i = (\alpha_i, \beta_i)^T$ represents a qubit on the chromosome before mutation, and $x_i' = (\alpha_i', \beta_i')^T$ represents the qubit after mutation. The quantum mutation operation actually changes the state of the superposition of the qubit state, so that when the qubit is measured, the original tendency to collapse to the state $|1\rangle$ becomes the tendency to collapse to the state $|0\rangle$, or vice versa.

4. Numerical Results and Discussions

This section presents case study results to demonstrate the performance of the proposed MoQGA. In order to facilitate the evaluation of the waveform set, the objective functions *PCCR*, *PASR*, and *ISL* are expressed in dB.

4.1. Quaternary Phase Code Design

In this subsection, we demonstrate the multi-objective optimization capability of the proposed method by comparing with NSGA-II through a design case of quaternary phase set design problem. We also illustrate how the *PSL* and *ISL* of the non-dominated solutions obtained by MoQGA are calculated in our method. The *PSL* and *ISL* results obtained in the later subsections of numerical results are all calculated in this way.

The Pareto front obtained by MoQGA is compared with NSGA-II in Figure 7. The MoQGA and NSGA-II start with the same initial population, whose Pareto front is represented by green square dots. The result is obtained at the end of the 300-th generation. The phase code sequence set size M is set to 4, the sequence length N is set to 64 and the number of phase values K is set to 4 (That means MoQGA designs quaternary phase-coded waveform set). It can be seen that the Pareto front obtained by MoQGA has lower objective functions than NSGA-II, which is one of the state-of-the-art multi-objective optimization methods. The three views of the obtained Pareto front are shown in Figure 7b–d. From these results, we can see that MoQGA algorithm can push the Pareto front deeper to the left-bottom corner where the values of *PASR*, *PCCR* and *ISL* are better.

The non-dominated solutions on the Pareto front obtained by MoQGA are multiple phase code matrices, while the optimal solution obtained by Multi-CAN or BiST is a phase code matrix. The result in Figure 7 cannot be directly compared to two standard metrics of the iterative algorithm and phase-coded waveform set (Such as Legendre sequence [49] and CAZAC sequence [50–52]), which are $PSL = \max\{PCCR, PASR\}$ and *ISL*. This paper calculates the *PSL* and *ISL* value of each non-dominated solution. The optimal solution with the lowest *PSL* and *ISL* value is selected as the comparison to BiST, Multi-CAN and other state-of-the-art methods. The *PSL* and *ISL* metrics of a Pareto front are expressed by (34) and (35), denoted as PSL_{MoQGA} and ISL_{MoQGA}.

$$PSL_{\mathrm{MoQGA}} = \min_{x \in PF^*} \max[PCCR(X), PASR(X)] \tag{34}$$

$$ISL_{\mathrm{MoQGA}} = \min_{x \in PF^*} ISL(X) \tag{35}$$

Table 2 shows the objective function values of the 32 non-dominated solutions on the Pareto front in Figure 7. According to (34) and (35), the results are expressed as $PSL_{\mathrm{MoQGA}} = -14.16$ dB (Set 25) and $ISL_{\mathrm{MoQGA}} = 11.14$ dB (Set 30). Since the MoQGA obtains total 32 non-dominated solutions, different solution can be selected according to specific practical system requirements. For instance, the Set 1 has the lowest *PASR* (-16.83 dB) with high *PCCR* (-13.01 dB). When the system requires lower *PASR*, the Set 1 will be selected. Overall, every solution is non-dominated to each other, so each of them is better than other 31 solutions in a certain dimension of the multi-objective functions.

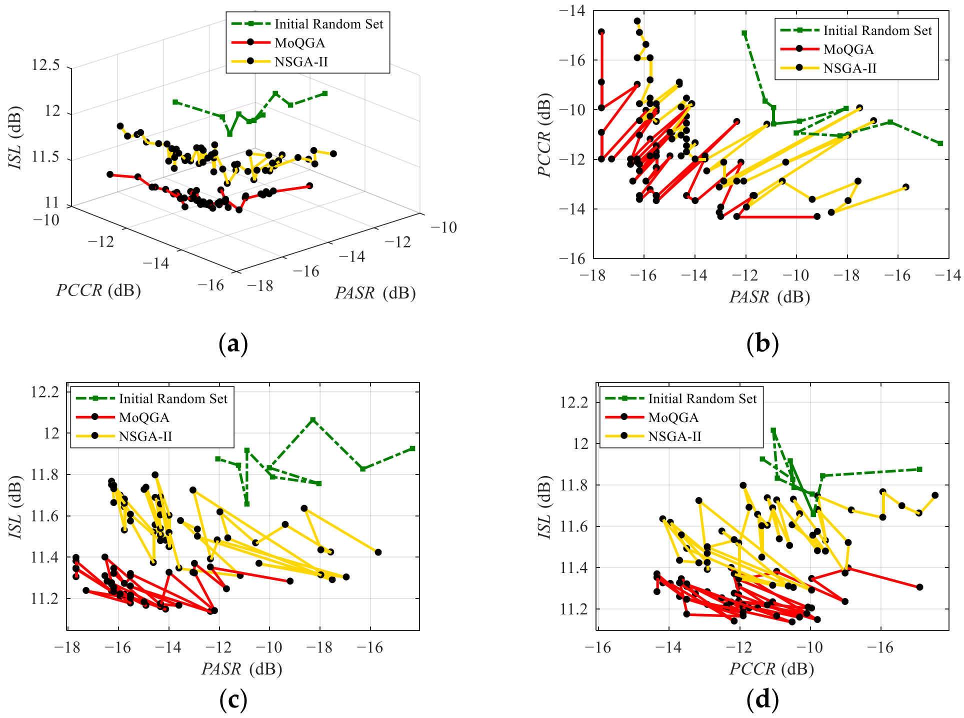

Figure 7. Pareto front obtained by MoQGA and NSGA-II when the parameters are M = 4, N = 64 and K = 4. (**a**) Pareto front; (**b**) *PCCR-PASR* of Pareto front; (**c**) *ISL-PCCR* of Pareto front; (**d**) *ISL-PASR* of Pareto front.

Table 2. Objective functions values of Pareto front.

No.	*PASR* (dB)	*PCCR* (dB)	*ISL* (dB)	No.	*PASR* (dB)	*PCCR* (dB)	*ISL* (dB)
Set 1	−16.83	−13.01	11.34	Set 17	−15.75	−12.04	11.17
Set 2	−16.83	−10.44	11.30	Set 18	−15.48	−12.94	11.18
Set 3	−16.63	−13.01	11.24	Set 19	−15.44	−12.47	11.16
Set 4	−16.28	−13.82	11.34	Set 20	−15.15	−13.74	11.17
Set 5	−16.26	−13.11	11.40	Set 21	−15.15	−12.14	11.16
Set 6	−16.21	−13.45	11.28	Set 22	−15.05	−11.89	11.15
Set 7	−16.12	−13.07	11.27	Set 23	−14.98	−13.84	11.32
Set 8	−16.12	−11.50	11.23	Set 24	−14.79	−12.94	11.16
Set 9	−16.08	−13.74	11.32	Set 25	−14.48	−14.16	11.37
Set 10	−16.08	−13.25	11.25	Set 26	−14.48	−13.98	11.32
Set 11	−16.08	−13.11	11.23	Set 27	−14.16	−14.16	11.35
Set 12	−15.95	−13.45	11.22	Set 28	−14.16	−12.25	11.13
Set 13	−15.95	−12.02	11.21	Set 29	−14.15	−14.08	11.32
Set 14	−15.87	−13.62	11.27	Set 30	−14.08	−13.07	11.14
Set 15	−15.75	−13.84	11.26	Set 31	−12.58	−14.16	11.28
Set 16	−15.75	−13.18	11.20	Set 32	−15.75	−12.04	11.17

4.2. Binary Code Design under Different Sequence Length N

In this subsection, we compare the MIMO radar binary phase-coded waveform set designed by the MoQGA with those designed by BiST, Multi-CAN, and Legendre sequence set. Notice that the objective function of the BiST is the weighted sum of the three objective functions [27], $\mathcal{F} = w_1 PCCR + w_2 PASR + w_3 ISL$. The BiST results under $w_1 = 0.25, w_2 = 0.25, w_3 = 0.5$ have the best metrics values, which are compared to

MoQGA in the later part of numerical results. The phase values of some sequence set are continuous. They are quantized into binary values at first. The design results are carried out under different code sequence length N, i.e., $N = \{8, 16, 24, 32, 40, 48, 56, 64\}$. The maximum generation of MoQGA is set to 300, and the number of individuals in the population is set to 100. Consider the two cases of $M = 3$ and $M = 4$, the following results are obtained over 10 trials. Figure 8 shows results under $M = 3$ and different sequence length while Figure 9 corresponds to $M = 4$.

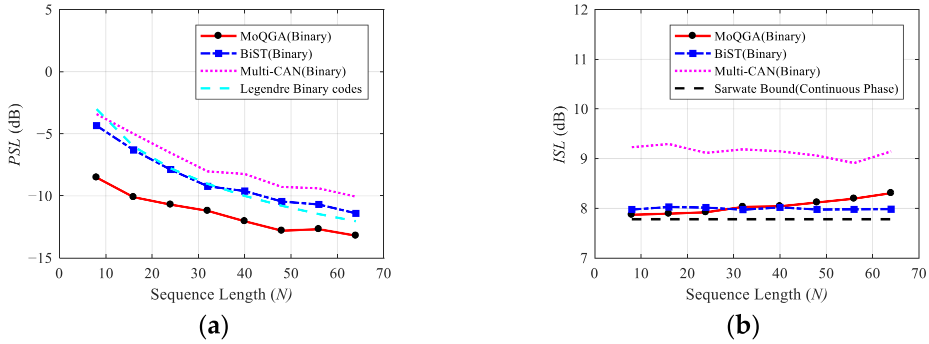

Figure 8. *PSL* and *ISL* values of MIMO radar binary phase code sequence set obtained by MoQGA and other methods under $M = 3$ and different code sequence length. (**a**) *PSL*; (**b**) *ISL*.

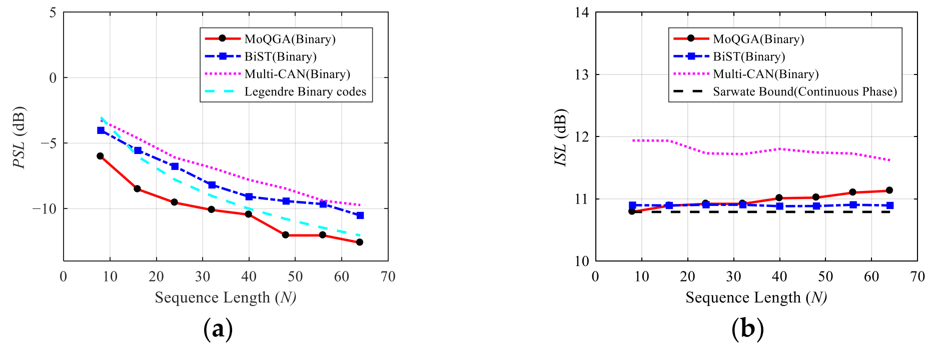

Figure 9. *PSL* and *ISL* values of MIMO radar binary phase code sequence set obtained by MoQGA and other methods under $M = 4$ and different code sequence length. (**a**) *PSL*; (**b**) *ISL*.

Figure 8a shows the result of *PSL* when $M = 3$. The red solid line represents the *PSL* value of the MIMO binary phase code sequence set designed by MoQGA. As the code sequence length N increases, the *PSL* value becomes smaller. The cyan dotted line represents the *PSL* value of the Legendre sequence, which is a structured MIMO binary phase code sequence set (The *PSL* value of Legendre sequence is $20\log_{10}(2/\sqrt{N})$ dB [53]). The pink dotted line represents the result of Multi-CAN, and the blue dotted line represents the result of BiST. It can be seen that the *PSL* value of the MIMO binary phase code sequence set designed by MoQGA is lower than the set designed by Multi-CAN, BiST and the Legendre sequence. Under the parameters set in this section, MoQGA's result is 2.64 dB lower than the Legendre sequence on average, 3.91 dB lower than Multi-CAN, and 2.66 dB lower than BiST.

Figure 8b shows the result of *ISL* when $M = 3$. The lower bound of the *ISL* value is $10\log_{10}(M(M-1))$ dB [15], and when $M = 3$, the lower bound is 7.78 dB, which is represented by the black dashed line in this figure. The red solid line represents the *ISL* values of binary phase code sequence set obtained by MoQGA. It can be seen that the *ISL* value increases with the increase of the code length N. The average value of *ISL* is 0.27 dB higher than the lower bound. The pink dotted line represents the result of Multi-CAN. It can be seen that the *ISL* value of the set obtained by MoQGA is 1.09 dB lower than that obtained by Multi-CAN on average. The blue dotted line represents the result of BiST and its *ISL* values are all around 8.00 dB, which is close to the lower bound. The result of MoQGA is 0.05 dB higher than BiST on average. However, for smaller N no larger than 40, the performance of MoQGA outperforms BiST by 0.04 dB. In conclusion, the *ISL* value of the MIMO code sequence set designed by the MoQGA is significantly better than that designed by Multi-CAN, slightly worse than BiST, but also close to the lower bound.

Figure 9a shows the similar result as Figure 8a when M = 4. The result shows that the *PSL* value of the MIMO binary phase code sequence set designed by MoQGA is 1.40 dB lower than the Legendre sequence on average, 3.14 dB lower than Multi-CAN, and 2.26 dB lower than BiST.

Figure 9b shows the similar result as Figure 8b when M = 4. At this time, the lower bound is 10.79 dB. The result of MoQGA is also compared with Multi-CAN and BiST. The result shows that the *ISL* value of the set designed by MoQGA is 0.81 dB lower than that of Multi-CAN on average, 0.07 dB higher than BiST, and only 0.18 dB higher than the lower bound. Regardless of the case of M = 3 or M = 4, as the code sequence length N increases, the *ISL* value of code sequence set obtained by MoQGA increases. That is because the degree of freedom of the phase code matrix increases as the N increases, but the maximum generation and number of individuals in population is not increased.

4.3. Quaternary Code Design under Different Sequence Length N

In this subsection, we evaluate the proposed method with quaternary code design. The results are shown in Figures 10 and 11, wherein except for the binary phase code changed to the quaternary phase code, the other parameters are the same as Figures 8 and 9. Figure 10 shows the *PSL* and *ISL* values of quaternary phase code sequence set designed by different algorithms under different code lengths when M = 3. The red solid line represents the result of the set designed by MoQGA. The trend of the curve is consistent with the situation of the binary phase code shown in Figure 8. The cyan dotted line represents the result of the CAZAC sequence. CAZAC sequence requires that the code sequence length is prime, so the result of CAZAC sequence is obtained when $N_{CAZAC} = \{7, 17, 23, 31, 41, 47, 53, 61\}$, the prime numbers close to the parameters of other code sequence set. In addition, because the phase values of CAZAC sequence are continuous, the phase values should be quantized into quaternary values at first.

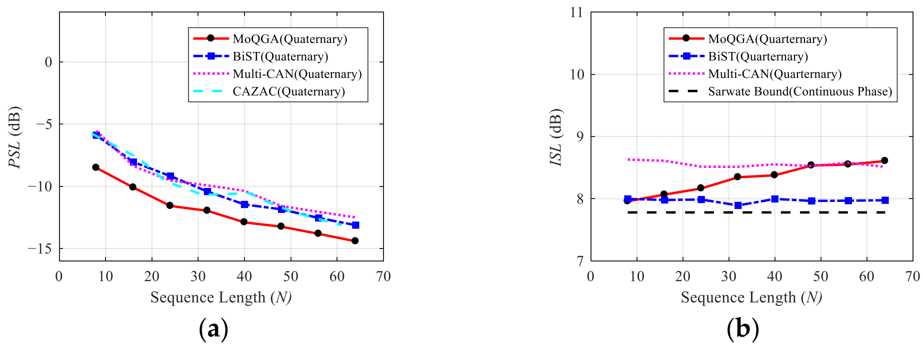

Figure 10. *PSL* and *ISL* values of MIMO radar quaternary phase code sequence set obtained by MoQGA and other methods under M = 3 and different code sequence length. (**a**) *PSL*; (**b**) *ISL*.

Figure 10a shows the *PSL* value of the MIMO quaternary phase code sequence set designed by MoQGA, which is 2.08 dB lower than Multi-CAN, 1.75 dB lower than BiST, and 1.89 dB lower than the CAZAC sequence on average. Figure 10b shows the *ISL* result when M = 3. The *ISL* result of MoQGA is 0.55 dB higher than the lower bound, 0.36 dB higher than BiST, and 0.23 dB lower than Multi-CAN.

Figure 11 shows the *PSL* and *ISL* results under different code lengths when M = 4. Figure 11a shows the *PSL* result. The result of MoQGA is 2.09 dB lower than Multi-CAN, 1.73 dB lower than BiST, and 1.65 dB lower than the CAZAC sequence on average.

Figure 11b shows the *ISL* result when *M* = 4. The result of MoQGA is 0.36 dB higher than the lower bound, 0.26 dB higher than BiST, and 0.24 dB lower than Multi-CAN.

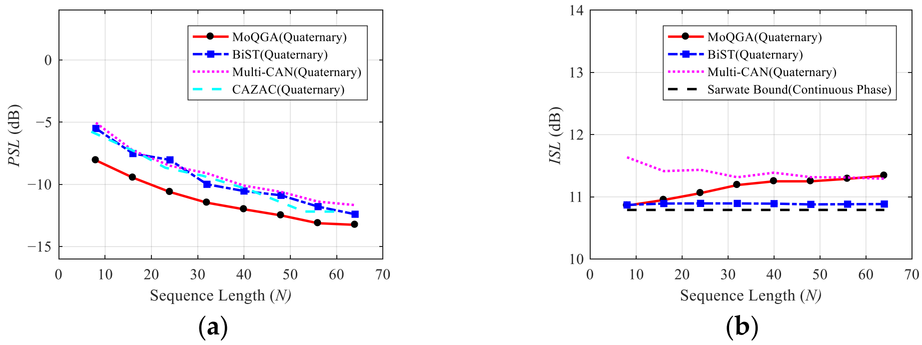

Figure 11. *PSL* and *ISL* values of MIMO radar quaternary phase code sequence set obtained by MoQGA and other methods under *M* = 4 and different code sequence length. (**a**) *PSL*; (**b**) *ISL*.

Comparing the results of quaternary code design with binary code design, we can see that when designing a quaternary phase code sequence set, the obtained *ISL* value of MoQGA is much higher than the binary case. And their trend via different sequence length *N* is the same. The *ISL* value increases as *N* increases. The results indicate that the *ISL* value results of MoQGA will become worse when the system's degree of freedom has increased while the maximum generation and number of the individuals in the population remain unchanged. This phenomenon is not obvious but also exists in the results of the *PSL* value results. Comparing the *PSL* results under binary and quaternary case, the binary phase code sequence set results of MoQGA are 2.66 dB and 2.26 dB lower than BiST respectively (corresponding to *M* = 3 and *M* = 4). However, the quaternary results are only 1.75 dB and 1.73 dB lower than BiST.

4.4. Impact of Sequence Set Size M

In order to analyze the impact of code sequence set size on the *PSL* and *ISL* result, the sequence design parameters are $N = 32,\ M = \{2,3,4,5,6,7,8\}$. The maximum generation is still set to 300, and the number of individuals in the population is still set to 100. The following results are still obtained over 10 trials.

Figure 12 shows the *PSL* and *ISL* values of MIMO binary phase code sequence set designed by different algorithms under different values of *M*. Figure 12a is the design result of *PSL* values. The *PSL* result of MoQGA is 1.14 dB lower than BiST, 2.83 dB lower than Multi-CAN on average. Figure 12b shows the result of the *ISL* values. For the seven values of *M* in this section, the lower bounds of the *ISL* values are 3.01 dB, 7.78 dB, 10.79 dB, 13.01 dB, 14.77 dB, 16.23 dB, and 17.48 dB respectively. On average, the result of MoQGA is 0.73 dB lower than Multi-CAN, 0.05 dB higher than BiST, and 0.16 dB higher than the lower bound.

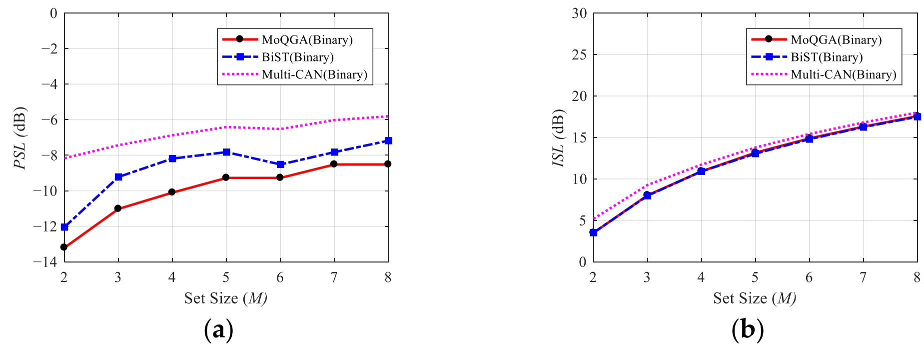

Figure 12. *PSL* and *ISL* values of MIMO radar binary phase code sequence set obtained by MoQGA and other methods under different sequence set size and *N* = 32. (**a**) *PSL*; (**b**) *ISL*.

Figure 13 shows the *PSL* and *ISL* results under quaternary case. It can be seen that the *PSL* value obtained by MoQGA is 0.95 dB lower than BiST, 1.83 dB lower than Multi-CAN. The result of *ISL* value is 0.22 dB lower than Multi-CAN, 0.22 dB higher than BiST, and 0.32 dB higher than the lower bound.

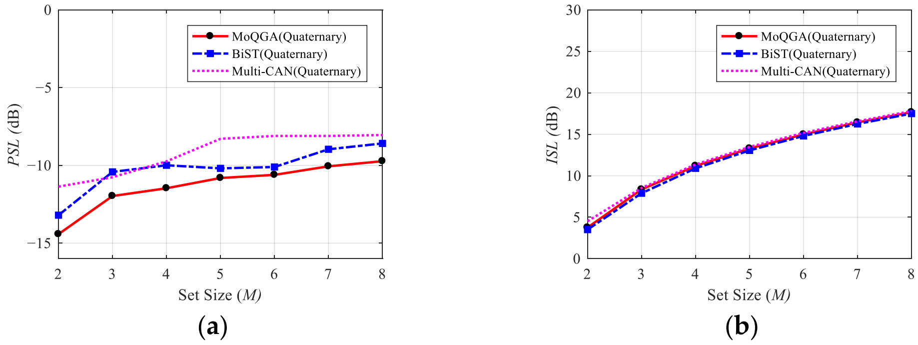

Figure 13. *PSL* and *ISL* values of MIMO radar quaternary phase code sequence set obtained by MoQGA and other methods under different sequence set size and $N = 32$. (**a**) *PSL*; (**b**) *ISL*.

It can be seen from Figures 12 and 13 that the *PSL* values and *ISL* values of the MIMO waveform set designed by different algorithms increase with the increase of the sequence set size. The design result of the quaternary phase code sequence set is lower than that of binary case. Although the *ISL* values of the waveform set designed by different algorithm are about the same, the *PSL* values obtained by MoQGA are lower than BiST and Multi-CAN.

4.5. Poly-Phase Code Design under Different K

In this subsection, code sequence length and set size are set to $N = 32$ and $M = 4$. The result is obtained under different number of phase values $K = \{2, 4, 8, 16, 32, 64\}$. Since the code length of CAZAC sequence should be prime number, set its length to $N = 31$. The max generation of MoQGA is still set to 300, and the number of individuals in the population is set to 100. The following result is still obtained over 10 trials.

Figure 14 shows the *PSL* values of phase code sequence set designed by different algorithms. As the number of phase values K increases from 2 to 64, the *PSL* value of the obtained phase code sequence set becomes smaller. From 2- to 4-phase code sequence set, the decline of the *PSL* value is most obvious. When $K = 8,16,32,64$, the *PSL* value has a small decrease relative to the 4-phase code sequence set. Apart from this result, the *PSL* value of the MIMO phase code sequence set designed by MoQGA is lower than BiST, Multi-CAN and quantized CAZAC sequence.

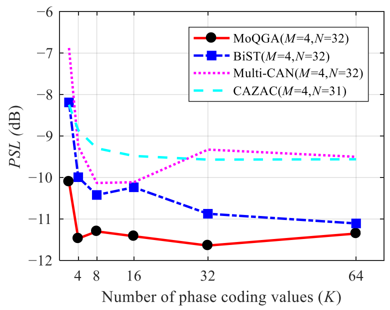

Figure 14. *PSL* values of MIMO radar poly-phase code sequence set obtained by MoQGA and other methods when $M = 4$ and $N = 32$.

4.6. Impact of Random Initialization

The initial population of the MoQGA is generated by random numbers. How random initialization affects the *PSL* metric and *ISL* metric is simulated here. The numerical simulations of this paper are implemented with MATLAB that runs on a PC with one Intel Core i7-6700 CPU and 8 GB RAM. When testing *PSL* and *ISL* metrics, the parameters are set as $M = 4$, $N = 64$, $K = 4$. The number of individuals is 100 and the maximum generation is 300. The results under the same parameters can also be seen in Figure 11, whose reported values are $PSL = -13.74$ dB and $ISL = 11.34$ dB. Then, 500 trials with random initial populations are calculated. The results are counted in Figures 15 and 16. It can be seen the distribution of the *PSL* and *ISL* metrics are concentrated. The average value of *PSL* is -13.68 dB; the standard deviation of the *PSL* is only 0.13 dB. The average value of *ISL* is 11.30 dB; the standard deviation of the *ISL* is only 0.03 dB. Red lines in Figures 15 and 16 represent the reported values in Figure 11. The results show that the random initializations only slightly affect the optimization results of the MoQGA.

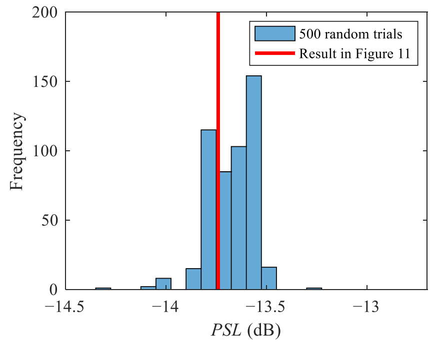

Figure 15. Histogram of the *PSL* values obtained over 500 random trials when the parameters are $M = 4$, $N = 64$, and $K = 4$.

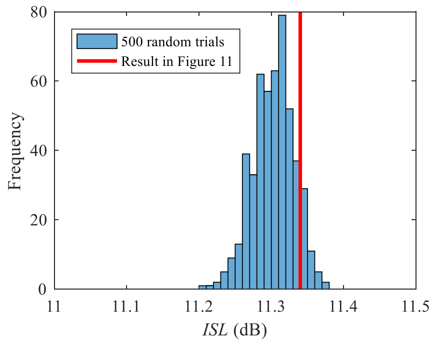

Figure 16. Histogram of the *ISL* values obtained over 500 random trials when the parameters are $M = 4$, $N = 64$, and $K = 4$.

4.7. Correlation Function of Phase Code Sequence Set

In this subsection, we discuss the performance of the proposed method in terms of *PCCR*. Figures 17 and 18 show the aperiodic auto- and cross-correlation functions of the phase code sequence set designed by MoQGA and BiST under $M = 4$, $N = 32$, and $K = 4$. Different from the experiments above, the results in Figures 17 and 18 are the best values selected from 10 trials. The peak value of aperiodic cross-correlation function of the waveform set obtained by BiST is 0.3125, and that of MoQGA is only 0.2519. Convert into dB form, the *PSL* value obtained by MoQGA is 1.87 dB lower than BiST. Lower aperiodic cross-correlation peak means that the interference between different waveforms of the MIMO radar system is lower. In addition, the solutions on the Pareto front obtained by MoQGA may have lower cross-correlation function. The radar system could choose a solution with lower cross-correlation peak, and then use weighted network, mismatch filtering, wavelet transform, or artificial neural network to suppress the side-lobe of the auto-correlation function [54–56].

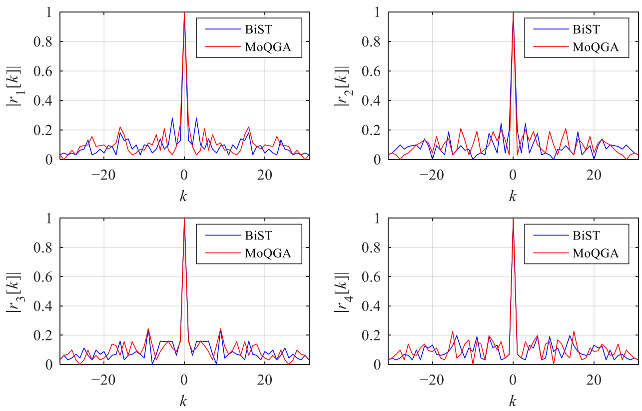

Figure 17. Auto-correlation functions of the waveform set obtained by MoQGA and BiST under $M = 4$, $N = 32$, and $K = 4$.

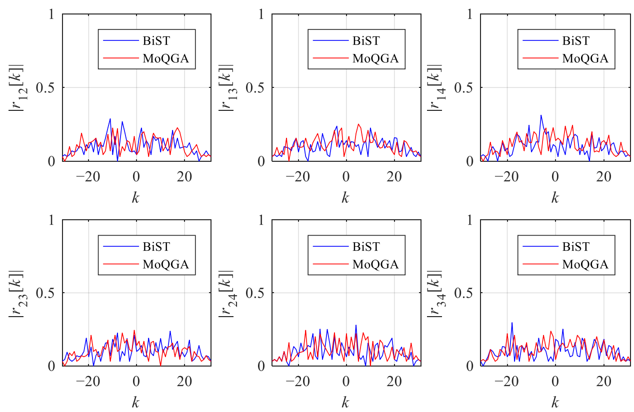

Figure 18. Cross-correlation functions of the waveform set obtained by MoQGA and BiST under $M = 4$, $N = 32$, and $K = 4$.

5. Conclusions

This paper proposes a new approach for MIMO radar phase-coded waveform design by formulating the waveform design problem into a multi-objective optimization problem. Subsequently, based on the Pareto dominance concept, combining the frameworks of NSGA-II and quantum-inspired genetic algorithm, this paper develops a multi-objective quantum genetic algorithm to solve the problem. Based on the Pareto level of the population, MoQGA was designed with unique quantum rotation and population update strategies. According to extensive numerical analysis, *PSL* values of the waveform set designed by MoQGA are 0.95–3.91 dB lower than Multi-CAN, BiST, and structured phase codes like CAZAC sequence and Legendre sequence. The obtained *ISL* values are close to the lower bound. The results under different waveform set parameters show that the gain decreases when the degree of freedom is large. A large number of trials prove that the results of the MoQGA are stable. MoQGA may be improved by adjusting the parameters of the MoQGA, like the population size and maximum generation.

Author Contributions: Conceptualization, T.L. and J.S.; methodology, T.L.; software, T.L.; validation, J.S., G.W. and Y.L.; formal analysis, G.W.; investigation, J.S.; resources, T.L.; data curation, T.L.; writing—original draft preparation, T.L.; writing—review and editing, J.S., G.W. and Y.L.; visualization, T.L.; supervision, J.S.; project administration, J.S.; funding acquisition, J.S. All authors have read and agreed to the published version of the manuscript.

Funding: This research was funded by the National Natural Science Foundation of China, Grant No. 62131001 and 62073334.

Data Availability Statement: Not applicable.

Conflicts of Interest: The authors declare no conflict of interest.

References

1. Gaji'c, A.; Radovanovi'c, J.; Vukovi´c, N.; Milanovi´c, V.; Boiko, D.L. Theoretical approach to quantum cascade micro-laser broadband multimode emission in strong magnetic fields. *Phys. Lett. A* **2021**, *387*, 127007. [CrossRef]
2. Pang, X.; Ozolins, O.; Zhang, L.; Schatz, R.; Udalcovs, A.; Yu, X.; Jacobsen, G.; Popov, S.; Chen, J.; Lourdudoss, S. Free-Space Communications Enabled by Quantum Cascade Lasers. *Phys. Status Solidi A* **2021**, *218*, 2000407. [CrossRef]
3. Spitz, O.; Herdt, A.; Wu, J.; Maisons, G.; Carras, M.; Wong, C.W.; Elsäßer, W.; Grillot, F. Private communication with quantum cascade laser photonic chaos. *Nat. Commun.* **2021**, *12*, 3327. [CrossRef] [PubMed]
4. Garlinska, M.; Pregowska, A.; Gutowska, I.; Osial, M.; Szczepanski, J. Experimental Study of the Free Space Optics Communication System Operating in the 8–12 µm Spectral Range. *Electronic* **2021**, *10*, 875. [CrossRef]
5. Lionis, A.; Peppas, K.; Nistazakis, H.E.; Tsigopoulos, A.D.; Cohn, K. Experimental Performance Analysis of an Optical Communication Channel over Maritime Environment. *Electronics* **2020**, *9*, 1109. [CrossRef]
6. Wang, Y.; Xu, H.; Li, D.; Wang, R.; Jin, C.; Yin, X.Y.; Gao, S.; Mu, Q.; Zuan, L.; Cao, Z. Performance analysis of an adaptive optics system for free-space optics communication through atmospheric turbulence. *Sci. Rep.* **2018**, *8*, 1124. [CrossRef]
7. Sun, H.; Gao, C.; The, K.C. Performance evaluation of practical MIMO radar waveforms. In Proceedings of the 2016 IEEE Radar Conference, Philadelphia, PA, USA, 2–6 May 2016; pp. 1–6.
8. Keel, B.M.; Baden, J.M.; Heath, T.H. A comprehensive review of quasi-orthogonal waveforms. In Proceedings of the 2007 IEEE Radar Conference, Waltham, MA, USA, 17–20 April 2007; pp. 122–127.
9. Pace, P. *Detecting and Classifying Low Probability of Intercept Radar*, 2nd ed.; Artech House: Norwood, MA, USA, 2008; pp. 358–377.
10. Bergin, J.; Guerci, J. *MIMO Radar: Theory and Application*; Artech House: Boston, MA, USA, 2018; pp. 45–49.
11. Deng, H. Polyphase code design for Orthogonal Netted Radar systems. *IEEE Trans. Signal Process.* **2004**, *52*, 3126–3135. [CrossRef]
12. Li, J.; Stoica, P. MIMO radar with colocated antennas. *IEEE Signal Process. Mag.* **2007**, *24*, 106–114. [CrossRef]
13. Friedlander, B. Waveform design for MIMO radars. *IEEE Trans. Aerosp. Electron. Syst.* **2007**, *43*, 1227–1238. [CrossRef]
14. Liu, H.; Zhou, S.; Zang, H.; Cao, Y. Two waveform design criteria for colocated MIMO radar. In Proceedings of the 2014 International Radar Conference, Lille, France, 13–17 October 2014; pp. 1–5.
15. Sarwate, D.V.; Pursley, M.B. Crosscorrelation properties of pseudorandom and related sequences. *Proc. IEEE* **1980**, *68*, 593–619. [CrossRef]
16. Welch, L. Lower bounds on the maximum cross correlation of signals (Corresp.). *IEEE Trans. Inf. Theory* **1974**, *20*, 397–399. [CrossRef]
17. Soltanalian, M.; Naghsh, M.M.; Stoica, P. On meeting the peak correlation bounds. *IEEE Trans. Signal Process.* **2014**, *62*, 1210–1220. [CrossRef]
18. Cao, S.; Madsen, N. Slow-time waveform design for MIMO GMTI radar using CAZAC sequences. In Proceedings of the 2018 IEEE Radar Conference, Oklahoma City, OK, USA, 23–27 April 2018; pp. 1456–1460.
19. Benedetto, J.J.; Donatelli, J.J. Frames and a vector-valued ambiguity function. In Proceedings of the 2008 42nd Asilomar Conf. on Signals, Systems and Computers, Pacific Grove, CA, USA, 26–29 October 2008; pp. 8–12.
20. He, H.; Stoica, P.; Li, J. Designing unimodular sequence sets with good correlations—Including an application to MIMO radar. *IEEE Trans. Signal Process.* **2009**, *57*, 4391–4405. [CrossRef]
21. Song, J.; Babu, P.; Palomar, D.P. Sequence set design with good correlation properties via majorization-minimization. *IEEE Trans. Signal Process.* **2016**, *64*, 2866–2879. [CrossRef]
22. Li, Y.; Vorobyov, S.A. Fast algorithms for designing unimodular waveform(s) with good correlation properties. *IEEE Trans. Signal Process.* **2018**, *66*, 1197–1212. [CrossRef]
23. Kerahroodi, M.A.; Aubry, A.; Maio, A.D.; Naghsh, M.M.; Hashemi, M.M. A coordinate-descent framework to design low PSL/ISL sequences. *IEEE Trans. Signal Process.* **2017**, *65*, 5942–5956. [CrossRef]
24. Wang, X.; Liu, H.; Yan, J.; Hu, L.; Bao, Z. Waveform design with low sidelobe and low correlation properties for MIMO radar. In Proceedings of the 2011 IEEE CIE International Conference on Radar, Chengdu, China, 24–27 October 2011; pp. 564–567.
25. Yang, Y.; Blum, R.S. MIMO radar waveform design based on mutual information and minimum mean-square error estimation. *IEEE Trans. Aerosp. Electron. Syst.* **2007**, *43*, 330–343. [CrossRef]
26. Sankuru, S.P.; Jyothi, R.; Babu, P.; Kerahroodi, M.A. Designing sequence set with minimal peak side-lobe level for applications in high resolution radar imaging. *IEEE Open J. Signal Process.* **2021**, *2*, 17–32. [CrossRef]
27. Kerahroodi, M.A.; Hashemi, M.M.; Naghsh, M.M. Designing sets of binary sequences for MIMO radar systems. *IEEE Trans. Signal Process.* **2019**, *67*, 3347–3360. [CrossRef]
28. Coello Coello, C.A. Evolutionary multi-objective optimization: A historical view of the field. *IEEE Comput. Intell. Mag.* **2006**, *1*, 28–36. [CrossRef]

29. Deb, K.; Pratap, A.; Agarwal, S.; Meyarivan, T. A fast and elitist multiobjective genetic algorithm: NSGA-II. *IEEE Trans. Evol. Comput.* **2002**, *6*, 182–197. [CrossRef]
30. Li, B.; Wang, L. A hybrid quantum-inspired genetic algorithm for multiobjective flow shop scheduling. *IEEE Trans. Syst. Man Cybern. Part B (Cybern.)* **2007**, *37*, 576–591. [CrossRef] [PubMed]
31. Han, K.H.; Kim, J.H. Quantum-inspired evolutionary algorithm for a class of combinatorial optimization. *IEEE Trans. Evol. Comput.* **2002**, *6*, 580–593. [CrossRef]
32. Jiang, S.; Yang, S. A strength Pareto evolutionary algorithm based on reference direction for multiobjective and many-objective optimization. *IEEE Trans. Evol. Comput.* **2017**, *21*, 329–346. [CrossRef]
33. Hamza, A.S.; Hamza, H.S.; El-Ghoneimy, M.M. Spectrum allocation in cognitive radio networks using evolutionary algorithms. In *Cognitive Radio and Its Application for Next Generation Cellular and Wireless Networks*; Venkataraman, H., Muntean, G.M., Eds.; Springer: Dordrecht, The Netherlands, 2012; Volume 116, pp. 259–285.
34. Yang, J.; Li, B.; Zhuang, Z. Multi-universe parallel quantum genetic algorithm its application to blind-source separation. In Proceedings of the International Conference on Neural Networks and Signal Processing 2003, Nanjing, China, 14–17 December 2003; pp. 393–398.
35. Zhang, Q.; Li, H. MOEA/D: A multiobjective evolutionary algorithm based on decomposition. *IEEE Trans. Evol. Comput.* **2007**, *11*, 712–731. [CrossRef]
36. Lellouch, G.; Mishra, A.K.; Inggs, M. Design of OFDM radar pulses using genetic algorithm based techniques. *IEEE Trans. Aerosp. Electron. Syst.* **2016**, *52*, 1953–1966. [CrossRef]
37. Xu, J.; Xu, J.; Dai, X.; Peng, Y. Using GA to design discrete frequency-coding waveform for orthogonal multistatic ISAR. In Proceedings of the 2007 1st Asian and Pacific Conference on Synthetic Aperture Radar, Huangshan, China, 5–9 November 2007; pp. 107–110.
38. Sen, S.; Tang, G.; Nehorai, A. Multiobjective optimization of OFDM radar waveform for target detection. *IEEE Trans. Signal Process.* **2011**, *59*, 639–652. [CrossRef]
39. Stringer, J.; Lamont, G.; Akers, G. Radar phase-coded waveform design using MOEAs. In Proceedings of the 2012 IEEE Congress on Evolutionary Computation, Brisbane, Australia, 10–15 June 2012; pp. 1–8.
40. O'Donnell, B.; Baden, J.M. Fast gradient descent for multi-objective waveform design. In Proceedings of the 2016 IEEE Radar Conference, Philadelphia, PA, USA, 2–6 May 2016; pp. 1–5.
41. Eedara, I.P.; Amin, M.G.; Hoorfar, A. Optimum code design using genetic algorithm in frequency hopping dual function MIMO radar communication systems. In Proceedings of the 2020 IEEE Radar Conference, Florence, Italy, 21–25 September 2020; pp. 1–6.
42. Xin, W.; Fujimura, S. Parallel quantum evolutionary algorithms with client-server model for multi-objective optimization on discrete problems. In Proceedings of the 2012 IEEE Congress on Evolutionary Computation, Brisbane, Australia, 10–15 June 2012; pp. 1–8.
43. Li, Y.; Wu, X.; Zhang, Y. A real-coded multi-objective quantum-inspired evolutionary algorithm and its application. In Proceedings of the 2017 29th Chinese Control and Decision Conference, Chongqing, China, 28–30 May 2017; pp. 848–852.
44. Park, I.; Lee, K.; Kim, J. Multi-objective evolutionary algorithm-based optimal posture control of humanoid robots. In Proceedings of the 2012 IEEE Congress on Evolutionary Computation, Brisbane, Australia, 10–15 June 2012; pp. 1–7.
45. Levanon, N.; Mozeson, E. *Radar Signals*; Wiley: Hoboken, NJ, USA, 2004; pp. 20–52.
46. Ko, K.-I.; Lin, C.-L. *Minimax and Applications. Nonconvex Optimization and Its Applications*; Springer: Boston, MA, USA, 1995; pp. 219–239.
47. Kennedy, J.; Eberhart, R. Particle swarm optimization. In Proceedings of the ICNN'95—International Conference on Neural Networks, Perth, Australia, 27 November–1 December 1995; pp. 1942–1948.
48. Beth, T. Quantum computing: An introduction. In Proceedings of the 2000 IEEE International Symposium on Circuits and Systems (ISCAS), Geneva, Switzerland, 28–31 May 2000; pp. 735–736.
49. Zhang, G.; Zhou, Q. Pseudonoise codes constructed by legendre sequence. *Electron. Lett.* **2002**, *38*, 376–377.
50. Chu, D. Polyphase codes with good periodic correlation properties (Corresp.). *IEEE Trans. Inf. Theory* **1972**, *18*, 531–532. [CrossRef]
51. Benedetto, J.J.; Konstantinidis, I.; Rangaswamy, M. Phase-coded waveforms and their design. *IEEE Signal Process. Mag.* **2009**, *26*, 22–31. [CrossRef]
52. Budišin, S.; Spasojević, P. Björck sequence sets. *Electron. Lett.* **2011**, *47*, 491–493. [CrossRef]
53. Han, Y.K.; Yang, K. New M-ary sequence families with low correlation and large size. *IEEE Trans. Inf. Theory* **2009**, *55*, 1815–1823. [CrossRef]
54. Rihaczek, A.W.; Golden, R.M. Range sidelobe suppression for Barker codes. *IEEE Trans. Aerosp. Electron. Syst.* **1971**, *AES-7*, 1087–1092. [CrossRef]
55. Ackroyd, M.H.; Ghani, F. Optimum mismatched filters for sidelobe suppression. *IEEE Trans. Aerosp. Electron. Syst.* **1973**, *AES-9*, 214–218. [CrossRef]
56. Kwan, H.K.; Lee, C.K. A neural network approach to pulse radar detection. *IEEE Trans. Aerosp. Electron. Syst.* **1993**, *29*, 9–21. [CrossRef]